RESEARCH ARTICLE

Check for updates

Reversible "on−off" conversion and ultra-high temperature sensitivity of a zero-dimensional lead-free Cs$_2$InBr$_5$(H$_2$O):Sb^{3+} perovskite†

Maohao Yang,[a] Wanyin Ge, [ID] *[a] Kenshi Matsumoto,[b] Masaki Saruyama, [ID] [b] Ryota Sato, [ID] [b] Haruka Takekuma, [ID] [b] Ryo Takahata [ID] [b] and Toshiharu Teranishi [ID] [b]

Zero-dimensional (0D) lead-free perovskites have garnered significant attention due to their unique opto-electronic properties and non-toxicity. However, the single response to stimuli in lead-free perovskites limits the versatility of multifunctional compounds. In this study, we abandoned the toxic bromic acid and utilized water as the reaction medium, to achieve an environmentally friendly green chemical route. We successfully prepared a zero-dimensional lead-free halide Cs$_2$In$_{1−x}$Sb$_x$Br$_5$(H$_2$O) perovskite with a fractal structure using an *in situ* solution crystallization method. Herein, we discovered that the recrystallization occurred beneath the smooth-grown rhombic crystal surface, forming fractal branched crystals. Interestingly, reversible luminescence color transitions from orange-red to yellow and return to the initial state were achieved in response to the individual stimuli of temperature and humidity. We found that H$_2$O molecules played a crucial role in the color tuning, enabling reversible "on−off" switching modes with rapid modulation rates. Moreover, the 0D lead-free halide perovskite Cs$_2$InBr$_5$(H$_2$O):Sb^{3+} also exhibited excellent temperature sensitivity, with the relative sensitivity (S_R) reaching up to 9.39% K$^{−1}$. This study provides valuable insights for the further development of halide perovskites in design and application fields, laying a foundation for the development of multifunctional smart materials and temperature sensing applications.

1. Introduction

Recently, lead halide perovskites have shown excellent optoelectronic properties, with growing applications in various fields.[1−8] However, the toxicity of the lead element severely limits the practical application.[9−15] Consequently, the global academic community is deeply engaged in the development of lead-free perovskite compounds. Various synthetic methods have been developed to obtain a diverse array of morphologies (*e.g.*, nanocrystals, single-crystals, thin films, and powders) of lead-free halide perovskites.[16−22] Lead-free perovskite materials have gained widespread attention due to their superior optical properties and environmentally friendly nature. They are widely used in areas such as solar cells, photodetectors, light-emitting diodes, and lasers, bringing new development opportunities for modern optoelectronic technology.[23−26] However, the innovative synthesis route and optical characteristics of the zero-dimensional (0D) indium-based halide perovskite

Cs$_2$InBr$_5$(H$_2$O), as well as its intrinsic physicochemical properties, still require further investigation.[27]

Currently, the incorporation of dopants is recognized as an effective strategy for improving the luminescence efficiency of perovskites.[28] Substantial advancements have been achieved in the study of the photoluminescence (PL) properties of indium-based halide perovskites doped with antimony (Sb^{3+}). For instance, Sb^{3+}-doping in 0D Cs$_2$SnCl$_6$ exhibits yellow-red emission.[29,30] Compared to the undoped counterparts, the photoluminescence quantum yield (PLQY) of Sb^{3+}-doped A$_2$InCl$_5$(H$_2$O) (A = Rb, Cs) has significantly improved, increasing from below 2% to a range of 85–95%.[31] In the family of Cs$_2$InX$_5$(H$_2$O) (X = Cl$^−$, Br$^−$ and I$^−$), the octahedral units exhibit pronounced electron–phonon coupling, resulting in a substantial Stokes shift observed in these 0D perovskite compounds.[32] Substitution of the halide from Cl$^−$ to Br$^−$ and I$^−$ also leads to redshifts in the photoluminescence (PL) and photoluminescence excitation (PLE) spectra of Sb^{3+}-doped Cs$_2$InX$_5$(H$_2$O) compounds.[33] Additionally, applying high pressure enables precise modulation of the PL properties of Cs$_2$InBr$_5$(H$_2$O), culminating in the observation of anomalous anti-Stokes emission.[34] In Cs$_2$InBr$_5$(H$_2$O), photogenerated charge carriers are spatially confined within isolated octahedra, enhancing the radiative recombination probability.[35−38] A-site cations have a slight effect on PL,[39] while water mole-

[a] School of Materials Science and Engineering, Shaanxi University of Science and Technology, Xi'an, Shaanxi 710021, P. R. China. E-mail: gewanyin@sust.edu.cn
[b] Institute for Chemical Research, Kyoto University, Gokasho, Uji, Kyoto 611-0011, Japan
†Electronic supplementary information (ESI) available. See DOI: https://doi.org/10.1039/d4qi01164c

cules, through their induced distortion of In^{3+} octahedra, result in a broad emission and exert a more pronounced influence on the self-trapped excitons (STEs).[40]

Halide perovskites are well recognized for their high sensitivity to environmental conditions, including air composition (humidity, oxygen), temperature, light exposure, and electric fields, which can lead to rapid degradation and limit their practical applications.[41–46] Fortunately, the novel lead-free 0D halide perovskite $Cs_2InBr_5(H_2O)$ stands out for its exceptional stability and tunable crystal structure. Interestingly, its isolated octahedral structure incorporates a water molecule (H_2O). As the temperature increases, the water molecule is released, modulating its luminescence from red to yellow.[47,48] Furthermore, when the dehydrated octahedral structure is subjected to an atmosphere with 80% relative humidity (RH), the PL wavelength and intensity undergo gradual alterations, with the color transitioning reversibly from yellow back to red.[49]
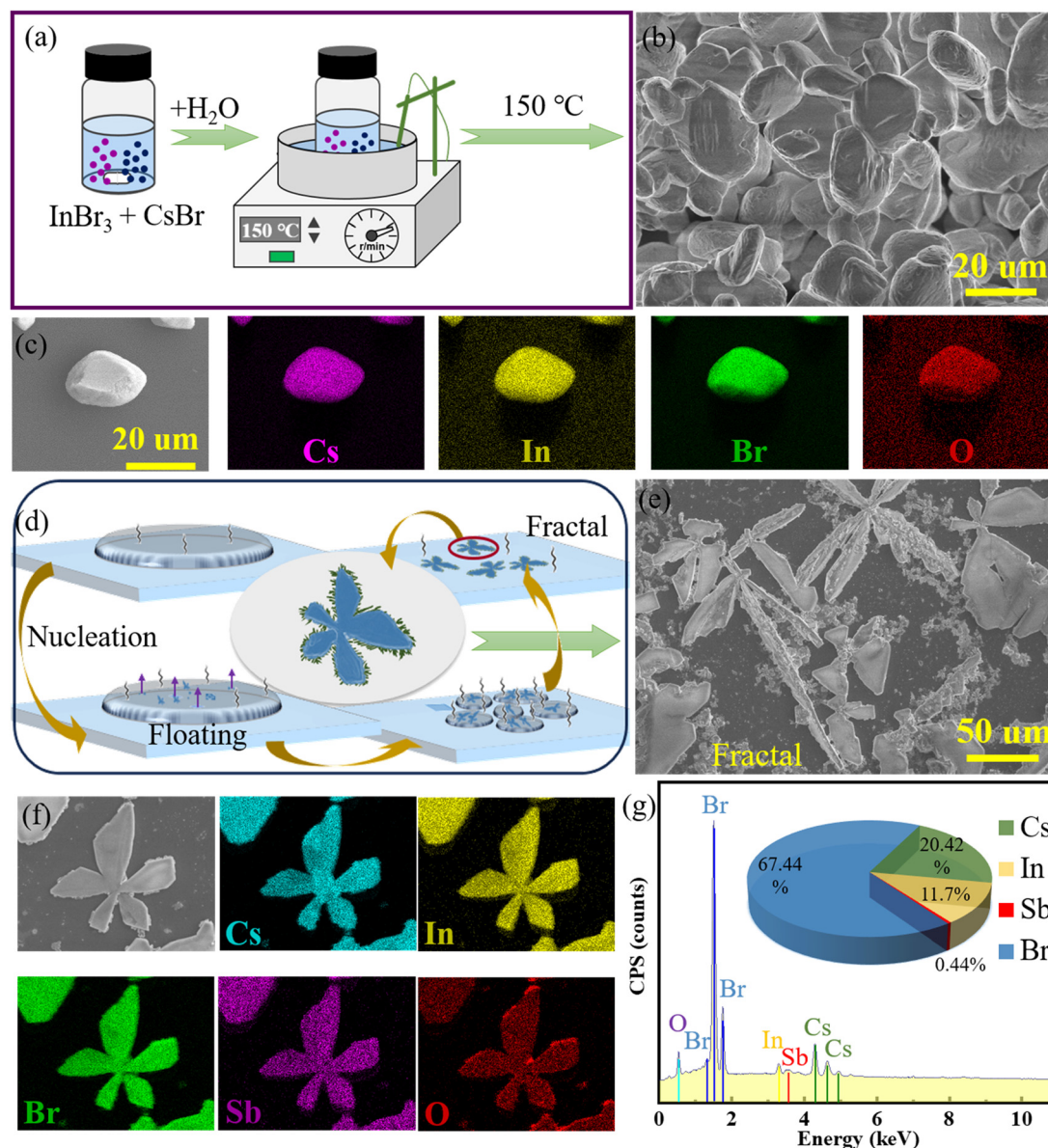
High-performance functional compounds that are reversible and responsive to stimuli such as temperature or humidity are highly desirable for sophisticated anti-counterfeiting technologies. However, many existing anti-counterfeiting functional compounds exhibit limited temperature responsiveness and necessitate further development to enhance their reversibility. In this study, we report the successful synthesis of a 0D halide perovskite, $Cs_2In_{1-x}Sb_xBr_5(H_2O)$, utilizing water as the reaction medium, thus abandoning the common chemical route involving bromic acid reported in the literature and demonstrating an environmentally friendly and green chemical approach. Furthermore, the diverse luminescence properties of $Cs_2InBr_5(H_2O){:}Sb^{3+}$ are of significant importance. We observed that the water molecule in the $Cs_2InBr_5(H_2O){:}Sb^{3+}$ molecular structure acts as a switch, facilitating an "on–off–on" cycle that can be repeated multiple times. We conducted in-depth analysis of the reversible structural and photoluminescence transitions triggered by water molecules or thermal effects. This halide perovskite, with its reversible photoluminescence properties, offers a fresh perspective, overcoming the limitations of traditional materials that exhibit singular responses. Additionally, we assessed the absolute sensitivity (S_A) and relative sensitivity (S_R) during temperature variations, with S_A achieving a maximum value of 3.55% K^{-1} and S_R reaching a peak of 9.39% K^{-1}, indicating extremely high sensitivity. These research findings demonstrate the high sensitivity and responsiveness of $Cs_2InBr_5(H_2O){:}Sb^{3+}$ to temperature changes within a certain temperature range, providing strong support for its applications in temperature- and humidity-sensitive fields. The reversibility of water molecules as switches and their multiple cycling capabilities presented in this study bring new opportunities for the development of lead-free 0D halide perovskites. This material, with its reversible photoluminescence characteristics, holds promise as a crucial component in anti-counterfeiting technology and multifunctional smart materials, while also exhibiting significant potential in high-performance temperature sensing applications.

2. Results and discussion

During the synthesis process, as depicted in Fig. 1a, distilled water was utilized as the solvent to formulate a transparent precursor solution by reacting $InBr_3$ (1 mmol, 99%, Sigma-Aldrich), CsBr (2 mmol, 99.9%, Sigma-Aldrich), and an appropriate amount of $SbBr_3$ (99.9%, Wako Pure Chemical Corporation), without using bromic acid, to achieve a green synthetic route. The scanning electron microscopy (SEM) image in Fig. 1b illustrates the morphological features of the synthesis reaction at 150 °C for 2 min, clearly displaying granular grains with sizes around 20 μm. An individual microcrystal in Fig. 1c exhibits its energy dispersive X-ray spectroscopy (EDX) features. Hydrogen (H), the lightest element, is typically undetectable by this method. The EDX spectrum confirms the homogeneous distribution of Cs, In, Br, and O elements and indicates elemental molar ratios approximating the stoichiometry of $Cs_2InBr_5(H_2O)$, thereby validating the successful synthesis of the $Cs_2InBr_5(H_2O)$ compound.

Figure 1d demonstrates crystallization near room temperature (around 30 °C), where the evaporative concentration of the solution droplets on glass slides leads to the emergence of dendritic crystals at the solution–glass interface. Subsequently, diamond-shaped, rectangular, and blade-like crystals nucleate and grow on the solution surface, eventually aggregating and overlaying to form butterfly-petal-shaped crystals. Notably, as the solution evaporates, leaving a partial liquid beneath the petal-shaped crystals, the solute concentration increases, altering the crystal growth conditions and kinetics, resulting in the growth of fractal dendritic crystals beneath the crystal surface, consistent with the recent literature.[50] The resulting fractal structure consists of an upper-layer butterfly petal-shaped crystal and a lower-layer dendritic crystal (Fig. 1e). ESI Fig. S1b† exhibits fractal structures obtained *via* the *in situ* solution method at different temperatures. The increasing temperature correlates with a decrease in the grain size and a corresponding increase in the quantity. This trend is attributed to the accelerated evaporation rate of water molecules at elevated temperatures, which in turn shortens the duration of crystal growth. Fig. 1f displays the EDX mapping characterizing the elemental composition and distribution of petal-shaped fractal structures, with the expected elements Cs, In, Sb, Br, and O. In Fig. 1g, the elemental molar ratio Cs : In : Br = 2 : 1 : 6, implying bromine ions exceeding the stoichiometric value, is potentially attributable to defects within the fractal structure, which could account for the slight deviations or fluctuations in the chemical stoichiometry of the crystal structure.

To ascertain the 0D halide perovskite structure of the as-prepared compound, we conducted X-ray diffraction (XRD) analysis. Subsequently, the high-precision XRD data were refined to validate the compound's phase and crystallographic characteristics. The refinement results, as presented in Fig. 2a, perfectly matched the synthesized sample's XRD pattern with the PDF card (01-087-4184) for $Cs_2InBr_5(H_2O)$, with an R_{wp} value of 6.44% and a goodness-of-fit factor of 1.52, signifying a high degree of fitting accuracy. The crystallographic para-

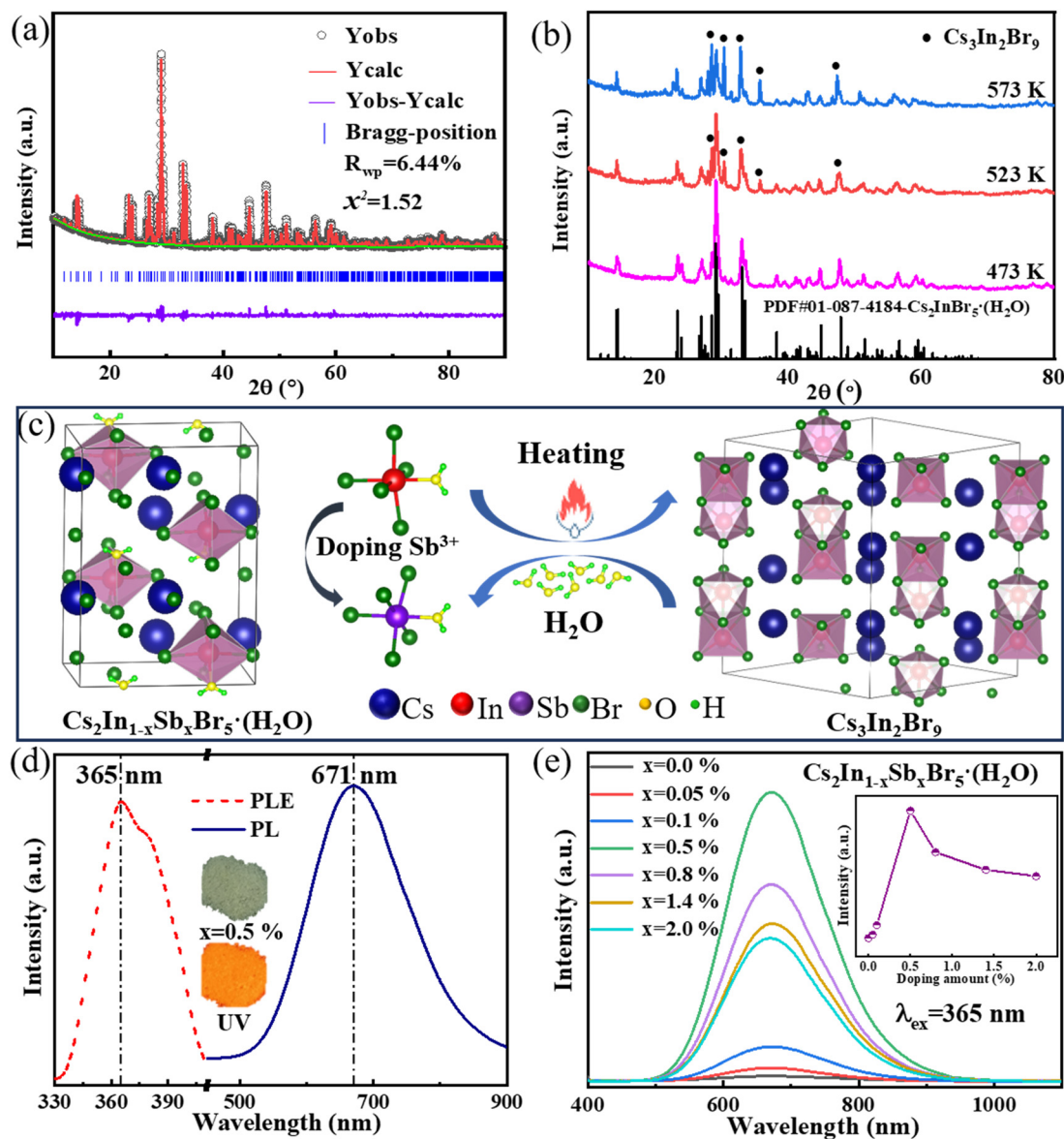This journal is © the Partner Organisations 2024

Inorg. Chem. Front., 2024, **11**, 5536–5545 | **5537**

Fig. 1 (a) Preparation process of Cs$_2$InBr$_5$(H$_2$O); (b) SEM image of Cs$_2$InBr$_5$(H$_2$O) prepared at 150 °C; (c) EDX mapping of Cs, In, Br, and O elements; (d) fractal structure of Cs$_2$In$_{1−x}$Sb$_x$Br$_5$(H$_2$O) samples obtained *via* the *in situ* solution crystallization method; (e) SEM image of the fractal structure post-crystallization; the EDX mapping (f) and EDX spectrum (g) of Cs$_2$InBr$_5$(H$_2$O):Sb.

meters derived were a = 14.8763 Å, b = 10.8116 Å, and c = 7.6437 Å, consistent with the *pnma* space group. Additionally, we observed a color change in the luminescence of Cs$_2$InBr$_5$(H$_2$O):Sb^{3+} under UV light after annealing at different temperatures. To further investigate this phenomenon, temperature-dependent XRD tests were conducted. As depicted in Fig. 2b, significant structural differences were evident in the samples annealed at different annealing temperatures. On increasing the temperature, the intensity of the diffraction peaks of Cs$_2$InBr$_5$(H$_2$O) gradually decreased, accompanied by the appearance of diffraction peaks corresponding to the Cs$_3$In$_2$Br$_9$ phase. This fact indicates that with increasing temperature, water molecules are progressively released from

Cs$_2$InBr$_5$(H$_2$O), leading to the partial transformation of Cs$_2$InBr$_5$(H$_2$O) into Cs$_3$In$_2$Br$_9$. Notably, this process is reversible, as the structure of the sample can be regenerated upon exposure to a humid environment.

The octahedral structure in the Cs$_2$InBr$_5$(H$_2$O):Sb^{3+} perovskite is composed of one indium (In) atom, five bromine (Br) atoms, and a single H$_2$O molecule, with indium atoms being partially substituted by Sb atoms, as illustrated in the crystal structure in Fig. 2c. Two Cs$^+$ ions are spatially separated, forming a 0D configuration. Upon exposure to thermal annealing, dehydration of the octahedral units occurs, prompting the reorganization of adjacent In–Br bonds and the formation of Cs$_3$In$_2$Br$_9$. Interestingly, the reverse transformation from

5538 | *Inorg. Chem. Front.*, 2024, **11**, 5536–5545

This journal is © the Partner Organisations 2024

Fig. 2 (a) Rietveld refinement results of $Cs_2InBr_5(H_2O)$ samples; (b) XRD patterns after annealing at different temperatures; (c) schematic representation of the reversible transformation between $Cs_2InBr_5(H_2O)$ and $Cs_3In_2Br_9$ crystal structures; (d) excitation (red line) and emission (blue line) spectra of $Cs_2InBr_5(H_2O):Sb^{3+}$ (inset: photograph of the 0.5% Sb^{3+} sample under ambient light and 365 nm UV light); (e) photoluminescence spectra of $Cs_2In_{1-x}Sb_xBr_5(H_2O)$ ($x = 0–2.0\%$), the inset shows the changes in Sb^{3+} doping concentration and PL intensity.

$Cs_3In_2Br_9$ back to $Cs_2InBr_5(H_2O)$ is feasible upon rehydration with water molecules. This reversible hydration–dehydration process can be represented by the formula:

$$2Cs_2InBr_5 \cdot (H_2O)(orange) \underset{+H_2O}{\overset{-H_2O}{\rightleftarrows}} Cs_3In_2Br_9(Yellow) + CsBr + 2H_2O. \quad (1)$$
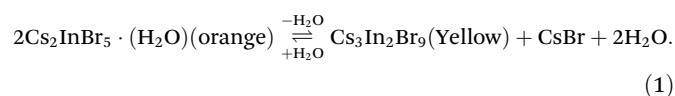
The successful utilization of an *in situ* solution crystallization method to prepare a 0D lead-free $Cs_2InBr_5(H_2O):Sb^{3+}$ halide perovskite is demonstrated. The structural transformation of the material is intimately associated with alterations in its color properties. The XRD patterns corresponding to

$Cs_2In_{1-x}Sb_xBr_5(H_2O)$ compounds ($x = 0–2.0\%$) are depicted in Fig. S2a.† These patterns reveal a close match between the diffraction peaks and those of the standard PDF card, indicating that introduction of Sb^{3+} as a dopant has a negligible impact on the overall crystal structure. Further examination of the XRD pattern at higher magnification, as shown in Fig. S2b,† unveils a noteworthy shift in diffraction peaks towards higher angles with increasing Sb^{3+} content. This shift can be attributed to the smaller ionic radius of Sb^{3+} (0.76 Å) compared to In^{3+} (0.80 Å), thereby suggesting that the doping concentration of Sb^{3+} exerts a subtle modulating effect on the structure.

Additionally, we observed that Sb^{3+}-doped $Cs_2InBr_5(H_2O)$ samples exhibit bright luminescence properties, characterized

by a visually perceptible "orange peel" color. To quantify this luminescence behavior, photoluminescence (PL) measurements were conducted. The photoluminescence excitation (PLE) spectrum in Fig. 2d presents a peak at 365 nm. Consequently, we selected 365 nm as the excitation source and observed an emission peak at 671 nm. Under identical conditions, the PL spectra of $Cs_2In_{1-x}Sb_xBr_5(H_2O)$ shown in Fig. 2e exhibit intense orange-red emissions for all samples. At a doping concentration of 0.5% Sb^{3+}, the emission intensity reaches its maximum. Therefore, the optimal doping concentration for $Cs_2In_{1-x}Sb_xBr_5(H_2O)$ is determined to be x = 0.5%, designated as the sample group with the best performance for subsequent temperature and humidity responsiveness assessments. Many studies indicate that self-trapped excitons (STEs) are the primary mechanism underlying the broad spectral emission in the 0D $Cs_2InBr_5(H_2O):Sb^{3+}$ perovskite.[38,51] As shown in Fig. S3,† the luminescence mechanism of the $Cs_2InBr_5(H_2O):Sb^{3+}$ perovskite involves the STE process.[33] Through coupling with polar lattice vibrations, excitons reduce the total energy of the system due to transient lattice deformations, thereby resulting in broad spectral emissions and larger Stokes shifts. Therefore, the luminescence of Sb^{3+} ions in $Cs_2InBr_5(H_2O):Sb^{3+}$ is attributed to the formation of STE. The emission peaks originate from the structural distortion of $Cs_2InBr_5(H_2O):Sb^{3+}$ crystals doped with Sb^{3+}, which promotes the emission of both singlet and triplet STEs.

We conducted a comprehensive study of the synthesized compound, $Cs_2InBr_5(H_2O):Sb^{3+}$, to assess its responsiveness to environmental changes by subjecting it to various temperature and humidity conditions. Fig. 3a shows the inscription of "SUST" on the sample after grinding the as-prepared powder

with ethanol. Upon exposure to UV lamp irradiation at room temperature, the emitted light from "SUST" appeared yellow, but it changed to orange-red under humid conditions. The intensity of the emitted light decreased with increasing temperatures, resulting in a state of fluorescence thermal quenching. As depicted in Fig. 2b, elevating the sample temperature to high degrees resulted in a structural transformation from the 0D perovskite $Cs_2InBr_5(H_2O)$ to the $Cs_3In_2Br_9$-type perovskite. *In situ* PL measurements under certain humidity conditions (as depicted in the inset of Fig. 3b) yielded the intensity-normalized spectrum. The PL emission peak migrated from 589 nm (red) to 671 nm (orange-red) over a period of 270 s, indicating a transition in color from yellow to orange-red light starting from 0 s after exposure to the humid environment. Furthermore, the response time for the transition from yellow to red light varies at different humidity levels. This is attributed to the formation of a distorted octahedral structure in $Cs_3In_2Br_9$, where the In–Br bonds form a regular octahedron. In contrast, $Cs_2InBr_5(H_2O):Sb^{3+}$ contains five Br ions and one H_2O, forming five In–Br bonds and one In–O bond, leading to a distorted octahedral structure. This distortion breaks the symmetry of $Cs_2InBr_5(H_2O):Sb^{3+}$ and results in a larger Stokes shift. Therefore, humidity levels during the reaction process are crucial for reversible processes.

Fig. 3c highlights the significant impact of environmental humidity on the luminescence properties of the material, with a notable emission peak shift observed at around 20 s from 597 nm to approximately 664 nm, accompanied by a gradual color change from yellow to orange-red, as depicted in the inset of Fig. 3c. Fig. S4a and b† show that an increase in dis-

Fig. 3 Sensitivity of $Cs_2InBr_5(H_2O):Sb^{3+}$ to water molecules. (a) Digital photograph of "SUST" under various conditions. (b) PL spectra variation in a humid environment; the illustration depicts the *in situ* testing process of PL. (c) Peak position as a function of exposure time to a humid environment (inset showing the color change of the sample's emission from 0 to 270 s). (d) CIE chromaticity diagram of the sample in a humid environment. The time-resolved PL decay curve for (e) $Cs_2InBr_5(H_2O):Sb^{3+}$ and (f) $Cs_3In_2Br_9$.

5540 | *Inorg. Chem. Front.*, 2024, **11**, 5536–5545

This journal is © the Partner Organisations 2024

tilled water content resulted in a redshift of the emission peak. The color alteration of $Cs_2InBr_5(H_2O):Sb^{3+}$ from green light to red light is shown in the digital photographs in Fig. S4c† after the addition of 0.05 mL of distilled water. This change further verifies the high sensitivity of $Cs_2InBr_5(H_2O):Sb^{3+}$ to humidity levels,[31] enabling precise control over the material's luminescence color, as shown in Fig. 3d. We characterized the fluorescence lifetimes of $Cs_2InBr_5(H_2O):Sb^{3+}$ (red light) and $Cs_3In_2Br_9$ (yellow light) to probe their photophysical properties. As shown in Fig. 3e and f, we observed a biexponential decay with an average lifetime of 0.909 μs for the 0D $Cs_2InBr_5(H_2O):Sb^{3+}$ perovskite, attributed to characteristic

singlet and triplet transitions of STEs. The average fluorescence lifetime of $Cs_3In_2Br_9$ decreased to 0.186 μs. Furthermore, in Fig. S5,† by employing the integrating sphere method, we measured the excitation and emission peaks, calculated the difference in their areas, and determined the photoluminescence quantum yields (PLQYs) of $Cs_2InBr_5(H_2O)$ and $Cs_3In_2Br_9$ to be 87.8% and 22.8%, respectively. This significant contrast suggests that water molecules (H_2O) may exert a notable influence on the PLQY of $Cs_3In_2Br_9$. Therefore, modulating the structure of $Cs_3In_2Br_9$ or doping specific ions could potentially enhance its luminescence performance, thereby increasing its practical utility.
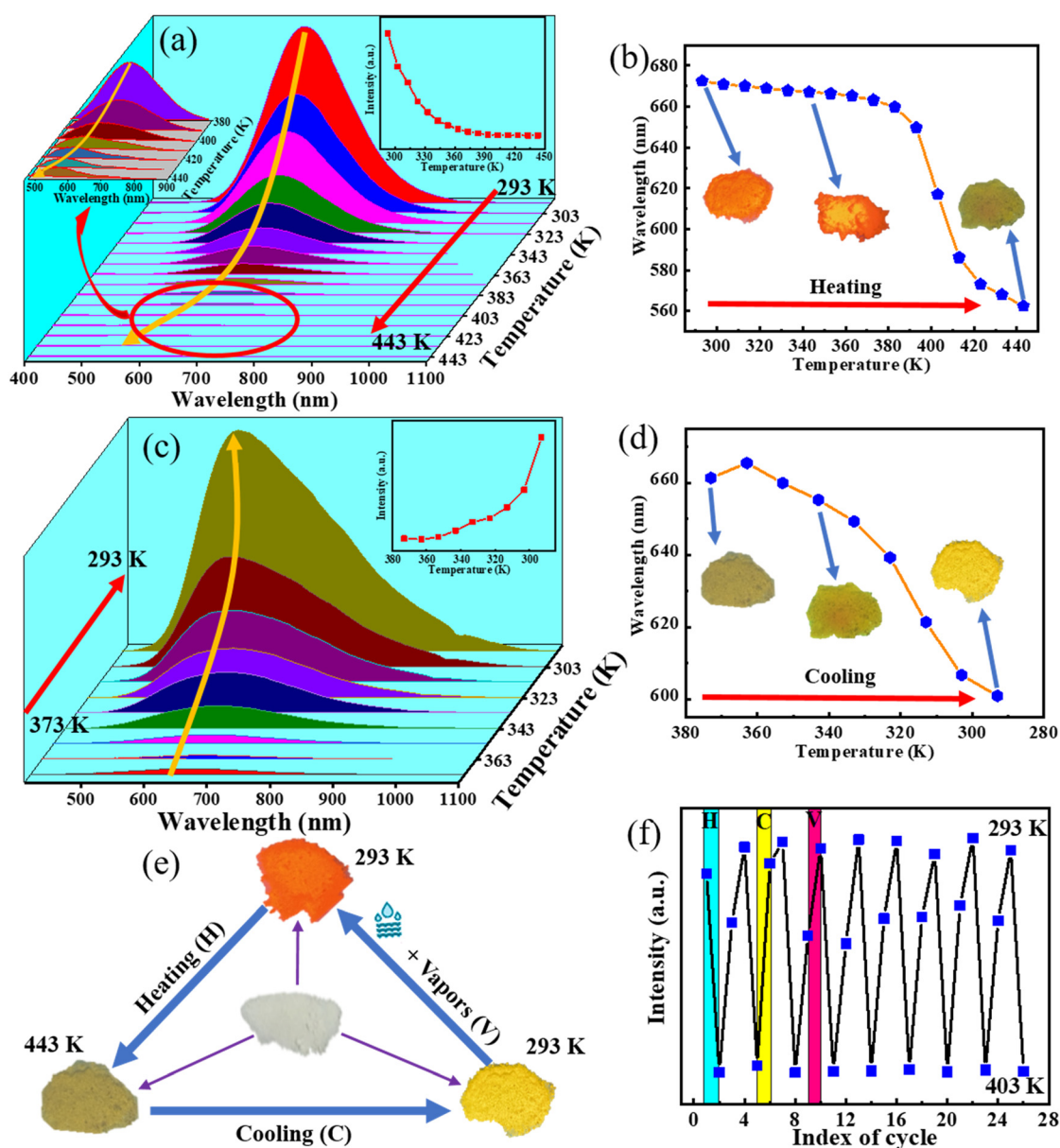
Fig. 4   (a) PL-temperature spectra of $Cs_2In_{0.995}Sb_{0.005}Br_5(H_2O)$ (inset: intensity *versus* temperature curve); (b) variation of the emission peak position during the heating process; (c) PL spectra during the temperature cooling process (inset: intensity *versus* temperature); (d) variation of the emission peak position during the cooling process; (e) color change of the sample during the cycling process; (f) changes in PL intensity during cycles of heating (H), cooling (C), and vapors (V).

In response to the temperature-induced alterations observed in $Cs_2InBr_5(H_2O):Sb^{3+}$, as depicted in Fig. 3a, we undertook an examination of the temperature-dependent photoluminescence (PL) spectra of $Cs_2In_{0.995}Sb_{0.005}Br_5(H_2O)$, spanning a temperature range of 293–443 K. As shown in Fig. 4a, the fluorescence intensity gradually decreases with increasing temperature. Concurrently, during the heating process, the emission peak gradually blue-shifts (Fig. 4b), and the full width at half maximum (FWHM) initially broadens and then narrows as illustrated in Fig. S6.† Fig. 4c depicts the cooling process, where the fluorescence intensity gradually increases as the temperature decreases, accompanied by a blue-shift in the emission peak (Fig. 4d), with the FWHM initially narrowing and then broadening. Fig. 4b and d insets illustrate that the sample emits orange-red light at room temperature. Upon heating to 443 K, faint yellow light is observed, and cooling back to room temperature emits bright yellow light. The cyclic process of heating (H), cooling (C), and vapors (V) of the $Cs_2In_{0.995}Sb_{0.005}Br_5(H_2O)$ sample is represented in Fig. 4e. The color change is attributed to the evaporation of water molecules from the molecular structure, leading to yellow light emission as the temperature increases. This process demonstrates reversibility, as samples emitting yellow light in a humid environment reverted to orange-red after a storage period. The temperature-dependent spectra in cycles of heating and cooling demonstrate good stability, as shown in Fig. S7.† This observation highlights the high sensitivity of $Cs_2In_{0.995}Sb_{0.005}Br_5(H_2O)$ to both temperature and humidity. The evaporation of water molecules causes the color changes. Water molecules play a crucial role in the color-changing process, allowing for repeatable and reversible color tuning. Fig. 4 shows the dynamic interaction between temperature, humidity, and molecular structure, highlighting the potential for further exploration in the manipulation and control of water molecules in these materials.

The compound's temperature sensing performance was determined using the fluorescence intensity variation shown in Fig. 4a. Given the material's broad single-peak emission profile, the conventional fluorescence intensity ratio (FIR) temperature calculation formula could not be utilized. Fig. 5a shows the fluorescence intensity values of the material at different temperatures, decreasing continuously with temperature elevation within the range of 293–413 K. By employing a nonlinear regression analysis of the data, the derived formula is:

$$I = A\exp(-T/B) + C. \tag{2}$$

The values for A, B, and C are 5.64×10^9, 28.55, and -3.41×10^3. These values can be utilized to analyze absolute sensitivity

Fig. 5 (a) Plot of intensity at different temperatures with nonlinear fitting curves; (b) S_A curve and S_R curve as a function of temperature.

Table 1 Temperature sensitivity performance of other luminescent materials

Samples	Temperature range (K)	S_{R-Max} temperature (K)	S_{R-Max} (% K^{-1})	Ref.
$Bi_2Ti_2O_7:Yb^{3+}/Er^{3+}$	298–540	298	1.53	54
$Cs_3Cu_2I_5:Mn^{2+}$	298–498	498	0.547	55
$CsPbCl_2Br:Eu^{3+}$	80–440	400	3.10	56
$NaYbF_4:Er^{3+}$	175–475	175	3.46	57
$CaTiO_3:Yb^{3+}/Er^{3+}$	303–523	303	1.17	58
$Cs_2Ag_{0.6}Na_{0.4}In_{0.9}Bi_{0.1}Cl_6$	300–470	345	1.05	59
$Cs_2NaYbCl_6:Er^{3+}/Sb^{3+}$	80–310	310	11.21	60
$Cs_4PbBr_6:Sm^{3+}$	303–423	303	3.83	61
$Cs_2InCl_5(H_2O):Te^{4+}$	80–380	320	6.2	62
$Cs_2InBr_5(H_2O):Sb^{3+}$	293–443	403	9.39	This work

(S_A) and relative sensitivity (S_R) using the following formulas:[52,53]

$$S_A = \frac{d(I(T)/I(0))}{dT} \quad S_R = S_A \frac{I(0)}{I(T)}. \quad (3)$$

The initial fluorescence intensity and the intensity corresponding to temperature T are represented by the symbols $I(0)$ and $I(T)$, respectively. S_A and S_R of the samples at different temperatures are shown in Fig. 5b, where $S_{A\text{-Max}}$ is 3.55% K^{-1}@293 K and $S_{R\text{-Max}}$ is 9.39% K^{-1}@403 K. The $S_{R\text{-Max}}$ achieved in this study is notably higher than those of other perovskites, as indicated by a comparison with literature values for other temperature sensing materials (refer to Table 1). This discrepancy suggests the potential importance of the $Cs_2InBr_5(H_2O){:}Sb^{3+}$ compound in temperature sensing applications, presenting new opportunities for the advancement of higher-performance temperature sensors and other optoelectronic devices due to its enhanced temperature sensitivity.

3. Conclusions

In our study, we synthesized a 0D halide perovskite using an environmentally friendly fabrication method, which revealed fractal structure growth through an *in situ* solution crystallization approach. Upon exposure to 365 nm UV excitation, the material exhibited an emission peak that could be tuned from 589 nm (yellow) to 671 nm (orange-red). Our confirm of the reversible structural and photoluminescence transitions triggered by water molecules or thermal reactions in the Sb^{3+}-doped $Cs_2InBr_5(H_2O)$. We found that heating the 0D $Cs_2In_{1-x}Sb_xBr_5(H_2O)$ perovskite leads to dehydration and transformation into the $Cs_3In_2Br_9$ structure. Notably, brief exposure to defined humidity levels (30 s) under specific relative humidity (RH) conditions reversed this transformation, reinstating the compound's original 0D configuration. By precisely manipulating temperature and humidity, we induced multiple color transitions in the material, revealing its versatile photoluminescence properties. This reversible photoluminescence behavior of the 0D lead-free halide perovskite sheds light on the structural and luminescence characteristics of the perovskite family, thereby broadening their prospective integration into reusable smart material systems. Furthermore, $Cs_2InBr_5(H_2O){:}Sb^{3+}$ exhibited remarkable temperature sensitivity, revealing a relative sensitivity (S_R) of 9.39% K^{-1}@403 K. The high sensitivity highlights the material's broad potential for temperature sensing applications, showcasing its adaptability in humidity- and temperature-sensitive systems.

Data availability

All relevant data are within the manuscript and its additional files. The data that support the findings of this study are available from the corresponding author upon reasonable request.

Conflicts of interest

There are no conflicts to declare.

Acknowledgements

References

1 S. Seth and A. Samanta, Photoluminescence of Zero-Dimensional Perovskites and Perovskite-Related Materials [J], *J. Phys. Chem. Lett.*, 2018, **9**(1), 176–183.

2 Y. Cun, Z. Yang, J. Li, *et al.*, Enhanced upconversion emission of three dimensionally ordered macroporous films $Bi_2Ti_2O_7{:}Er^{3+}$, Yb^{3+} with silica shell[J], *Ceram. Int.*, 2015, **41**(9), 11770–11775.

3 Y. T. Wu, D. Han, B. C. Chakoumakos, *et al.*, Zero-dimensional Cs_4EuX_6 (X = Br, I) all-inorganic perovskite single crystals for gamma-ray spectroscopy[J], *J. Mater. Chem. C*, 2018, **6**(25), 6647–6655.

4 Y. C. Hou, H. D. Wu, J. J. Yoon, *et al.*, Self-Assembly of 0D/3D Perovskite Bi-Layer from a Micro-Emulsion Ink[J], *Adv. Energy Mater.*, 2023, **13**(28), 2300570.

5 G. Q. Li, X. Chen, M. Wang, *et al.*, Regulating Exciton De-Trapping of Te^{4+}-Doped Zero-Dimensional Scandium-Halide Perovskite for Fluorescence Thermometry with Record High Time-Resolved Thermal Sensitivity[J], *Adv. Mater.*, 2023, **35**(44), 2305495.

6 Z. Ma, Z. Shi, D. Yang, *et al.*, Electrically-Driven Violet Light-Emitting Devices Based on Highly Stable Lead-Free Perovskite $Cs_3Sb_2Br_9$ Quantum Dots[J], *ACS Energy Lett.*, 2020, **5**(2), 385–394.

7 A. K. Tomar, A. Joshi, S. Atri, *et al.*, Zero-Dimensional Ordered $Sr_2CoMoO_{6-\delta}$ Double Perovskite as High-Rate Anion Intercalation Pseudocapacitance[J], *ACS Appl. Mater. Interfaces*, 2020, **12**(13), 15128–15137.

8 P. Du, L. Luo and W. Cheng, Neoteric Mn^{2+}–activated $Cs_3Cu_2I_5$ dazzling yellow–emitting phosphors for white–LED[J], *J. Am. Ceram. Soc.*, 2020, **103**(2), 1149–1155.

9 H. X. Wu, Z. X. Lin, J. Song, *et al.*, Boosting the Self-Trapped Exciton Emission in Cs_4SnBr_6 Zero-Dimensional Perovskite via Rapid Heat Treatment[J], *Nanomaterials*, 2023, **13**(15), 2259.

10 S. Bhaumik, A. Bruno and S. Mhaisalkar, Broadband emission from zero-dimensional Cs_4PbI_6 perovskite nanocrystals[J], *RSC Adv.*, 2020, **10**(23), 13431–13436.

11 K. N. Krishnakanth, S. Seth, A. Samanta, *et al.*, Broadband ultrafast nonlinear optical studies revealing exciting multiphoton absorption coefficients in phase pure zero-dimensional Cs_4PbBr_6 perovskite films[J], *Nanoscale*, 2019, **11**(3), 945–954.

This journal is © the Partner Organisations 2024

Inorg. Chem. Front., 2024, **11**, 5536–5545 | **5543**

12 B. A. Al-Asbahi, S. M. H. Qaid and A. S. A. Dwayyan, Effect of Donor-Acceptor Concentration Ratios on Non-Radiative Energy Transfer in Zero-Dimensional Cs_4PbBr_6 Perovskite/MEH-PPV Nanocomposite Thin Films[J], *Polymers*, 2020, **12**(2), 444.

13 S. Seth and A. Samanta, Fluorescent Phase-Pure Zero-Dimensional Perovskite-Related Cs_4PbBr_6 Microdisks: Synthesis and Single-Particle Imaging Study[J], *J. Phys. Chem. Lett.*, 2017, **8**(18), 4461–4467.

14 Y. T. Chen, X. T. Wang, Y. Wang, *et al.*, Functional organic cation induced 3D-to-0D phase transformation and surface reconstruction of $CsPbI_3$ inorganic perovskite[J], *Sci. Bull.*, 2023, **68**(7), 706–712.

15 Y. Kawano, A. Nakagawa, J. Chantana, *et al.*, Impacts of 0D Cs_4PbI_6 phase in all-inorganic $CsPbI_3$ perovskites on their physical, optical properties and photovoltaic performances [J], *Thin Solid Films*, 2022, **759**, 139485.

16 Y. Liu, X. Sun, Z. H. Gao, *et al.*, Zero-Dimensional Perovskite Open Cavities for Low-Threshold Stimulated Emissions[J], *J. Phys. Chem. C*, 2020, **124**(46), 25499–25508.

17 H. G. Zhao, R. J. Sun, Z. F. Wang, *et al.*, Zero-Dimensional Perovskite Nanocrystals for Efficient Luminescent Solar Concentrators[J], *Adv. Funct. Mater.*, 2019, **29**(30), 1902262.

18 L.-J. Chen, C.-R. Lee, Y.-J. Chuang, *et al.*, Synthesis and Optical Properties of Lead-Free Cesium Tin Halide Perovskite Quantum Rods with High-Performance Solar Cell Application[J], *J. Phys. Chem. Lett.*, 2016, **7**(24), 5028–5035.

19 M. Leng, Y. Yang, Z. Chen, *et al.*, Surface Passivation of Bismuth-Based Perovskite Variant Quantum Dots To Achieve Efficient Blue Emission[J], *Nano Lett.*, 2018, **18**(9), 6076–6083.

20 B. Pradhan, G. S. Kumar, S. Sain, *et al.*, Size Tunable Cesium Antimony Chloride Perovskite Nanowires and Nanorods[J], *Chem. Mater.*, 2018, **30**(6), 2135–2142.

21 J. C. Dahl, W. T. Osowiecki, Y. Cai, *et al.*, Probing the Stability and Band Gaps of $Cs_2AgInCl_6$ and $Cs_2AgSbCl_6$ Lead-Free Double Perovskite Nanocrystals[J], *Chem. Mater.*, 2019, **31**(9), 3134–3143.

22 J. Luo, X. Wang, S. Li, *et al.*, Efficient and stable emission of warm-white light from lead-free halide double perovskites[J], *Nature*, 2018, **563**(7732), 541–545.

23 L.-J. Chen, Synthesis and optical properties of lead-free cesium germanium halide perovskite quantum rods[J], *RSC Adv.*, 2019, **9**(58), 33847–33847.

24 F. De Angelis, The Prospect of Lead-Free Perovskite Photovoltaics[J], *ACS Energy Lett.*, 2021, **6**(4), 1586–1587.

25 L.-J. Chen, J.-H. Dai, J.-D. Lin, *et al.*, Wavelength-Tunable and Highly Stable Perovskite-Quantum-Dot-Doped Lasers with Liquid Crystal Lasing Cavities[J], *ACS Appl. Mater. Interfaces*, 2018, **10**(39), 33307–33315.

26 L.-J. Chen and J.-H. Dai, Growth, morphological and optical characteristics of ZnSSe nanorods[J], *Opt. Mater.*, 2017, **64**, 356–360.

27 J. Huang, T. Chang, R. Zeng, *et al.*, Controlled Structural Transformation in Sb-Doped Indium Halides A_3InCl_6 and $A_2InCl_5 \cdot H_2O$ Yields Reversible Green-to-Yellow Emission Switch[J], *Adv. Opt. Mater.*, 2021, **9**(13), 2002267.

28 X. Zhang, L. Li, Z. Sun, *et al.*, Rational chemical doping of metal halide perovskites[J], *Chem. Soc. Rev.*, 2019, **48**(2), 517–539.

29 Y. Jing, Y. Liu, J. Zhao, *et al.*, Sb^{3+} Doping-Induced Triplet Self-Trapped Excitons Emission in Lead-Free Cs_2SnCl_6 Nanocrystals[J], *J. Phys. Chem. Lett.*, 2019, **10**(23), 7439–7444.

30 J. Zhou, M. Li, M. S. Molokeev, *et al.*, Tunable photoluminescence in Sb^{3+}-doped zero-dimensional hybrid metal halides with intrinsic and extrinsic self-trapped excitons[J], *J. Mater. Chem. C*, 2020, **8**(15), 5058–5063.

31 P. G. Han, C. Luo, S. Q. Yang, *et al.*, All-Inorganic Lead-Free 0D Perovskites by a Doping Strategy to Achieve a PLQY Boost from <2% to 90%.[J], *Angew. Chem., Int. Ed.*, 2020, **59**(31), 12709–12713.

32 J. D. Majher, M. B. Gray, T. Liu, *et al.*, Rb_3InCl_6: A Monoclinic Double Perovskite Derivative with Bright Sb^{3+}-Activated Photoluminescence[J], *Inorg. Chem.*, 2020, **59**(19), 14478–14485.

33 Y. Jing, Y. Liu, X. Jiang, *et al.*, Sb^{3+} Dopant and Halogen Substitution Triggered Highly Efficient and Tunable Emission in Lead-Free Metal Halide Single Crystals[J], *Chem. Mater.*, 2020, **32**(12), 5327–5334.

34 Q. Li, B. Xu, Z. W. Chen, *et al.*, Excitation-Dependent Emission Color Tuning of 0D $Cs_2InBr_5 \cdot H_2O$ at High Pressure[J], *Adv. Funct. Mater.*, 2021, **31**(38), 2104923.

35 Y. Dong, T. Qiao, D. Kim, *et al.*, Precise Control of Quantum Confinement in Cesium Lead Halide Perovskite Quantum Dots via Thermodynamic Equilibrium[J], *Nano Lett.*, 2018, **18**(6), 3716–3722.

36 M. I. Saidaminov, J. Almutlaq, S. Sarmah, *et al.*, Pure Cs_4PbBr_6: Highly Luminescent Zero-Dimensional Perovskite Solids[J], *ACS Energy Lett.*, 2016, **1**(4), 840–845.

37 T. Jun, K. Sim, S. Iimura, *et al.*, Lead-Free Highly Efficient Blue-Emitting $Cs_3Cu_2I_5$ with 0D Electronic StructureStructure[J], *Adv. Mater.*, 2018, **30**(43), 1804547.

38 B. M. Benin, D. N. Dirin, V. Morad, *et al.*, Highly Emissive Self-Trapped Excitons in Fully Inorganic Zero-Dimensional Tin Halides[J], *Angew. Chem., Int. Ed.*, 2018, **57**(35), 11329–11333.

39 L. Xingyi, X. Xi, L. Ben, *et al.*, Antimony-Doping Induced Highly Efficient Warm-White Emission in Indium-Based Zero-Dimensional Perovskites[J], *CCS Chem.*, 2020, **2**, 216–224.

40 Q. Ge, R. Zheng, J. Lin, *et al.*, $Cs_2InCl_5(H_2O)$: A moisture-stable defective double halide perovskite analogue with broadband emission[J], *Mater. Lett.*, 2020, **277**, 128280.

41 G. Volonakis, A. A. Haghighirad, R. L. Milot, *et al.*, $Cs_2InAgCl_6$: A New Lead-Free Halide Double Perovskite with Direct Band Gap[J], *J. Phys. Chem. Lett.*, 2017, **8**(4), 772–778.

42 K. Jiang, L. Zhang, J. Lu, *et al.*, Triple-Mode Emission of Carbon Dots: Applications for Advanced Anti-

5544 | *Inorg. Chem. Front.*, 2024, **11**, 5536–5545

This journal is © the Partner Organisations 2024

Counterfeiting[J], *Angew. Chem., Int. Ed.*, 2016, **55**(25), 7231–7235.

43 B. Li, H.-T. Fan, S.-Q. Zang, *et al.*, Metal-containing crystalline luminescent thermochromic materials[J], *Coord. Chem. Rev.*, 2018, **377**, 307–329.

44 X. Li, Y. Wu, S. Zhang, *et al.*, CsPbX$_3$ Quantum Dots for Lighting and Displays: Room-Temperature Synthesis, Photoluminescence Superiorities, Underlying Origins and White Light-Emitting Diodes[J], *Adv. Funct. Mater.*, 2016, **26**(15), 2435–2445.

45 Z. Hu, B. J. Deibert and J. Li, Luminescent metal-organic frameworks for chemical sensing and explosive detection [J], *Chem. Soc. Rev.*, 2014, **43**(16), 5815–5840.

46 Z.-P. Wang, B. Hu, X.-H. Qi, *et al.*, Microwave-assisted ionothermal synthesis of a water-stable Eu-coordination polymer: a Ba^{2+} ion detector and fluorescence thermometer [J], *Dalton Trans.*, 2016, **45**(21), 8745–8752.

47 W. Z. Li, S. N. Zhu, Y. Y. Zhao, *et al.*, Structural, electrical, optical properties and stability of Cs$_2$InBr$_{5-y}$X$_y$H$_2$O (X = Cl, I, y=0, 1, 2, 3, 4, 5) perovskites: the first principles investigation[J], *Thin Solid Films*, 2021, **733**, 138805.

48 J. X. Wang, Y. F. Yuan, C. L. Liu, *et al.*, Pressure-induced emission enhancement with an abnormal blue shift of the Sb^{3+}-doped zero-dimensional lead-free halide perovskiteCs$_2$InBr$_5$·H$_2$O[J], *Phys. Rev. B*, 2023, **107**(21), 214111.

49 L. Zhou, J. F. Liao, Z. G. Huang, *et al.*, A Highly Red-Emissive Lead-Free Indium-Based Perovskite Single Crystal for Sensitive Water Detection[J], *Angew. Chem., Int. Ed.*, 2019, **58**(16), 5277–5281.

50 W. Y. Ge, M. H. Yang, M. Saruyama, *et al.*, Evolution of fractal patterns in lead-free, zero-dimensional perovskite Cs$_2$InBr$_5$(H$_2$O)[J], *CrystEngComm*, 2024, **26**(19), 2571–2576.

51 V. Morad, Y. Shynkarenko, S. Yakunin, *et al.*, Disphenoidal Zero-Dimensional Lead, Tin, and Germanium Halides: Highly Emissive Singlet and Triplet Self-Trapped Excitons and X-ray Scintillation[J], *J. Am. Chem. Soc.*, 2019, **141**(25), 9764–9768.

52 D. Das, S. L. Shinde and K. K. Nanda, Temperature-Dependent Photoluminescence of g-C$_3$N$_4$: Implication for Temperature Sensing[J], *ACS Appl. Mater. Interfaces*, 2016, **8**(3), 2181–2186.

53 J. S. Hu, X. M. Bian, R. N. Wang, *et al.*, Giant Enhancement in Upconversion Luminescence of β-Ba$_2$ScAlO$_5$:Yb^{3+}/Er^{3+} Phosphor by the Intermediate Band through Ca^{2+} Doping [J], *Chem. Mater.*, 2022, **34**(7), 3089–3098.

54 M. Xu, W. Ge, Y. Tian, *et al.*, Tunable upconversion luminescence and enhanced temperature sensitive properties from Bi$_2$Ti$_2$O$_7$:Yb^{3+}/Er^{3+} nanofibers[J], *J. Mater. Sci.*, 2021, **56**(15), 9302–9314.

55 P. Du, P. Cai, W. Li, *et al.*, Ratiometric optical thermometer based on the use of manganese(II)-doped Cs$_3$Cu$_2$I$_5$ thermochromic and fluorescent halides[J], *Microchim. Acta*, 2019, **186**(11), 730.

56 Y. Yu, G. Shao, L. Ding, *et al.*, Ultra-stable Eu^{3+}-doped CsPbCl$_2$Br$_1$ perovskite quantum dots glass for optical temperature sensing[J], *J. Rare Earths*, 2021, **39**(12), 1497–1505.

57 D. Baziulyte-Paulaviciene, N. Traskina, R. Vargalis, *et al.*, Thermal decomposition synthesis of Er^{3+}-activated NaYbF$_4$ upconverting microparticles for optical temperature sensing[J], *J. Lumin.*, 2019, **215**, 116672.

58 S. Pattnaik and V. K. Rai, Impact of charge compensation on optical and thermometric behaviour of titanate phosphors[J], *Mater. Res. Bull.*, 2020, **125**, 110761.

59 H. Xu, J. Yu, Q. Hu, *et al.*, Highly Sensitive Dual-Mode Optical Thermometry of Er^{3+}/Yb^{3+} Codoped Lead-Free Double Perovskite Microcrystal[J], *J. Phys. Chem. Lett.*, 2022, **13**(4), 962–968.

60 Z. Wang, Y. Wang, Y. Jing, *et al.*, Bi^{3+}/Sb^{3+}-doped Cs$_2$Na(Yb/Er)Cl$_6$ double perovskite nanocrystals: Fabrication, optical properties and temperature sensing[J], *J. Lumin.*, 2024, **267**, 120389.

61 G. Yao, S. Li, D. Valiev, *et al.*, Luminescence behavior and temperature sensing properties of Sm^{3+}-doped Cs$_4$PbBr$_6$ quantum dots encapsulated in borogermanate glass[J], *J. Non-Cryst. Solids*, 2022, **582**, 121462.

62 J.-H. Wei, J.-B. Luo, J.-F. Liao, *et al.*, Te^{4+}-doped Cs$_2$InCl$_5$·H$_2$O single crystals for remote optical thermometry[J], *Sci. China Mater.*, 2022, **65**(3), 764–772.

This journal is © the Partner Organisations 2024

Inorg. Chem. Front., 2024, **11**, 5536–5545 | **5545**